Assessment of URANS Modeling of Dynamic Stall via Reynolds Stress Tensor Perturbations

Federico Vegetti
Leonardo
Rome, Italy

Giulio Gori
Politecnico di Milano
Milan, Italy

ABSTRACT

We explore diverse strategies to perform a credibility assessment of predictions from the unsteady Reynolds-Averaged Navier-Stokes (URANS) model. In particular, we consider the epistemic uncertainty in the turbulence closure and compute uncertainty estimates using the Eigenspace Perturbation Method. The novelty lies in the application, which regards unsteady use cases of interest to aeronautics. The time-series of predicted quantities of interest are subject to Power Spectral Density and coherence analysis. Results show that the credibility assessment should consider multiple quantities of interest at once.

NOTATION

Here, the list of Symbols and Acronyms used is reported.

*

Symbols

C_L Lift Coefficient

C_m Moment Coefficient

C_p Pressure Coefficient

k Turbulent Kinetic Energy

R_{ij} Reynolds Stress Tensor

u Freestream Velocity

*

Acronyms

CFD Computational Fluid Dynamics

CFL Courant Number

DeepDS Deep Dynamic Stall

DES Detach Eddy Simulation

DSV Dynamic Stall Vortex

EPM Eigenspace Perturbation Method

LES Large Eddy Simulation

LightDS Light Dynamic Stall

LSV Shear Layer Vortex

PSD Power Spectral Density

RANS Reynolds-Averaged Navier-Stokes

SST Shear Stress Transport

TKE Turbulent Kinetic Energy

URANS Unsteady Reynolds-Averaged Navier-Stokes

INTRODUCTION

Computational Fluid Dynamic (CFD) based on the Reynolds-Averaged Navier-Stokes (RANS) model is possibly the most popular approach in aeronautics. However, RANS predictions are poorly credible with regards to certain applications e.g., the ones entailing a strongly separated flow. Part of the reason lies in the need of turbulence closures to approximate the Reynolds Stress Tensor (RST) resulting from the time-averaging of the Navier-Stokes equations. Indeed, closures are semi-empirical and subject to a substantial uncertainty inherent to the structure of their own equations.

In rotorcraft aerodynamics, the accurate prediction of the dynamic stall remains a major computational challenge. Due to its balance between computational cost and accuracy, the Unsteady RANS model (URANS) is commonly used to investigate dynamic stall. As reported by A. Klein, K. Richter, A. Gardner, A. Altmikus, T. Lutz and E. Krämer (Ref. 15), to perform rotor performance analysis, empirical dynamic stall models are often used in blade element momentum codes, whereas a large number of turbulence closures are employed in steady and unsteady numerical simulation with varying degree of success. It follows that RANS predictions are affected by an amount of uncertainty that modelers should try to quantify.

This work aims to investigate the credibility of URANS in the context of dynamic stall by roughly estimating the prediction uncertainty due to the turbulence closure. To achieve this goal, we take advantage of the Eigenspace Perturbation Method (EPM) implemented via the EQUiPS (Ref. 3) module in the SU2 solver (Ref. 1). Previous applications of the EPM involve steady cases of academic interest, see (Refs. 2,3) among others, or unsteady flows developing around a fixed geometry, see (Refs. 4, 18). Here, we apply the EPM to a pitching airfoil i.e., a moving geometry. Two case studies are examined: the deep dynamic stall of the OA209 airfoil and the light dynamic stall of the NACA 23012 airfoil. It must be stressed that we are not interested in computing provable uncertainty bounds, something the EPM is not capable of (Ref. 14), but rather we provide an estimation of the possible prediction dispersion caused by the uncertainty in unsteady application, similar to (Ref. 4). For both application cases, our study includes the comparison of Power Spectral Density (PSD) and coherence of the time signals obtained from perturbing the Reynolds Stress Tensor (RST) according to the standard EPM (Ref. 2). The aim is to establish the credibility of CFD simulations in capturing key aerodynamic characteristics.

In Sec. *METHODOLOGY*, we explain the EPM and the approach used to investigate unsteady applications; an exemplary steady test is also reported for verification purposes. Sec. *RESULTS* describes the unsteady applications i.e., the analysis of a deep and a light dynamic stall, and reports the corresponding credibility assessment. Lastly, Sec. *CONCLUSIONS* reports the conclusions of this work.

METHODOLOGY

Turbulence closures approximate the Reynolds stress tensor in terms of mean flow quantities; using the eigenvalue decomposition, the symmetric Reynolds stress tensor can be written as

$$R_{ij} = 2k\left(\frac{\delta_{ij}}{3} + v_{in}\Lambda_{nl}v_{lj}\right), \qquad (1)$$

where k is the turbulent kinetic energy, v is the matrix of eigenvectors, and Λ is the diagonal matrix of eigenvalues of the Reynolds stress tensor R_{ij}.

The eigenvalues are ordered so that $\lambda_1 \geq \lambda_2 \geq \lambda_3$. The amplitude, shape, and orientation of the Reynolds stress are explicitly represented by k, λ_i, and v_{ij}, respectively. The objective is to determine the possible Reynolds stresses, perturbing eigenvalues and eigenvectors of Eq. 1.

The perturbations to the eigenvalues Λ are conveniently defined in a barycentric map with coordinates x, assuming $\lambda_i^* = B^{-1}x^*$. The perturbed quantities are indicated by *, whereas B is the transformation from the eigenvalue space to the barycentric framework. In the barycentric framework, it is possible to define a triangular region including all the physically meaningful realizations of the Reynolds Stress Tensor. Indeed, by definition, the tensor must be positive semi-definite. The eigenvalue perturbation in the baricentric map has both a direction and a magnitude. Considering the extreme states of Reynolds stresses, the three vertices of the triangle x_{1C}, x_{2C} and x_{3C} represent the one-, two- and three-component (*1C*, *2C*, and *3C*) limiting states of turbulence componentiality. The magnitude of the perturbation in the barycentric triangle is represented by $\Delta_B \in [0,1]$. Therefore, the perturbed barycentric coordinates x^* are given by

$$x^* = x + \Delta_B(x^t - x), \qquad (2)$$

where x^t denotes the target vertex (representing one of the *1C*, *2C* or *3C* limiting states) and x is the baseline model prediction. Using $\Delta_B = 1$, the three limiting states are considered.

Virtually, all RANS closures consider the turbulent kinetic energy evolution that satisfies the general form (Eq. 3), directly derived from the Navier-Stokes equations for an incompressible fluid

$$\frac{\partial k}{\partial t} + U_j\frac{\partial k}{\partial x_j} = -\frac{\partial T_i}{\partial x_i} + \mathscr{P} - \varepsilon, \qquad (3)$$

T is the turbulent transport process, ε is the dissipation rate, and $\mathscr{P}$ is the production process. The method proposed in (Ref. 2) focuses on a purely physical approach, exploiting the perturbation of the alignment of the eigenvectors to modulate the production term $\mathscr{P}$. Specifically, the perturbation targets the value of the Frobenius inner product $\langle A,R\rangle_F = \mathrm{tr}(AR)$, where A is the mean velocity gradient and R is the Reynolds stress tensor, seeking the extreme states of production (maximum and minimum). The tightest bounds for $\langle A,R\rangle_F$, along with their respective alignments, can be determined. These are given by

$$\langle A,R\rangle_F \in [\lambda_1\gamma_3 + \lambda_2\gamma_2 + \lambda_3\gamma_1, \lambda_1\gamma_1 + \lambda_2\gamma_2 + \lambda_3\gamma_3], \qquad (4)$$

where $\gamma_1 \geq \gamma_2 \geq \gamma_3$ are the eigenvalues of the symmetric component of A (mean rate of strain tensor).

In practice, perturbations to the Reynolds Stress Tensor are injected at each iteration of the CFD solver. First, the barycentric coordinate of the eigenvalues computed using the baseline model is perturbed to force the realization of one *1C*, *2C* or *3C* extremal states. Note that the baseline model can be any turbulence closure. Once the extremal state (or any arbitrary point between the baseline coordinate and the vertex, depending on Δ_B) is imposed, a perturbation is applied to rotate the eigenvectors. The methodology can be interpreted as the reshaping and reorienting of the ellipsoid associated with the Reynolds stress tensor. That is, changing the state of the components modifies the shape of the ellipsoid, whereas perturbing the eigenvectors corresponds to rotating the ellipsoid. Together, these two perturbations enable us to maximize the information we may get from single-point statistics and estimate the uncertainty bounds.

In summary, the EPM UQ framework requires to evaluate five extreme states of the Reynolds stress tensor that stem from the combination of eigenvalues and eigenvectors perturbations. These correspond to three extreme states of the component (*1C*, *2C*, *3C*) and two extreme alignments of the Reynolds stress eigenvectors ($v_{\min}, v_{\max}$). For the *3C* limiting state, the Reynolds stress ellipsoid is perfectly spherical, hence no changes are obtained using the eigenvector perturbation. Thus, a set of five RANS simulations is needed to estimate the uncertainty. In a steady RANS simulation, the credibility of the results can be quantified using the average value of the quantity of interest across the five simulations. By calculating the difference between the maximum and minimum values of a generic Quantity of Interest p, a prediction dispersion, denoted δ, can be estimated

$$\delta = \max(p^{1C}, p^{2C}, p^{3C}, p^{p1c1}, p^{p1c2}) - \min(p^{1C}, p^{2C}, p^{3C}, p^{p1c1}, p^{p1c2}). \quad (5)$$

The term δ serves as an indicator of the variability, or spread, of the quantity of interest among the five simulations, providing insight into the uncertainty associated with the simulation results.

For unsteady simulations there is no clear strategy for quantifying the URANS model credibility w.r.t. the turbulence closure. As a starting point, the average value of quantity of interest can be considered and compared among the different simulations. Moreover, following the approach used by G. Gori, O. P. Le Maître and P. M.Congedo (Ref. 4), it is possible to consider the power spectral density (PSD) and coherence of the six signals (baseline and five perturbations).

PSD could be used as an indicator of differences in terms of energy distribution among harmonics, and if the signals show a similar energy distribution at the same frequencies, this could be a good indicator of similarity, while differences in peaks and distribution could suggest lower similarity.

Coherence represents the correlation between two signals as a function of frequency and can be interpreted as a measure of their similarity in terms of the distribution of spectral energy. In practical terms, coherence acts as an indicator to determine whether the signals share a similar structure in the frequency components.

The EPM is implemented into the EQUiPS (Ref. 3) module of the SU2 open-source suite (Ref. 1), which is employed hereinafter to investigate the use cases. The EQUiPS module allows to estimate the uncertainties arising from RANS turbulence closures using arbitrary perturbations along the junction line between the baseline barycentric coordinate and any of the three vertices. Additionally, the EQUiPS module allows the permutation of the eigenvector components to introduce a binary perturbation of their orientation. Overall, five type of perturbations of the baseline closure are possible to obtain estimates about the uncertainty affecting the selected quantities of interest. For each, any value of Δ_B, see Eq. (2), can be applied to estimate δ.

Application to a steady case

Using the EQUiPS module, the EPM is applied to investigate the steady flow around the classical NACA 0012 airfoil. The large amount of experimental data available is a consistent reference for assessing RANS CFD simulations against wind tunnel tests. Our study considers the airfoil Angle of Attack (AOA, α) as a sweep parameter.

The test conditions are summarized in Tab. 1.

Parameter	Value
Freestream Temperature	300 K
Freestream Mach Number	0.15
Angle of Attack (AOA)	0°–20°
Reynolds Number	6.0×10^6
Reynolds Length	1.0 m

Table 1. Simulation parameters used for the analysis from (Ref. 3).

The farfield boundary is placed 500 times the length of the (1 m) chord from the airfoil. On the surface of the airfoil, a no-slip condition is imposed. The mesh is a structured C-grid provided by the *SU2* test case repository, which also provides computational data for additional comparison. An enlargement of the airfoil region is shown in Fig. 1. The CFD configuration file is also provided by the *SU2* test case and uses the SST turbulence closure as the baseline for the EQUiPS module. The EQUiPS under-relaxation factor is set to 0.1, whereas the magnitude of perturbation is set to $\Delta_B = 1$. All possible extreme perturbation and the correspondent setting option used in the configuration file are reported in Tab. 2.

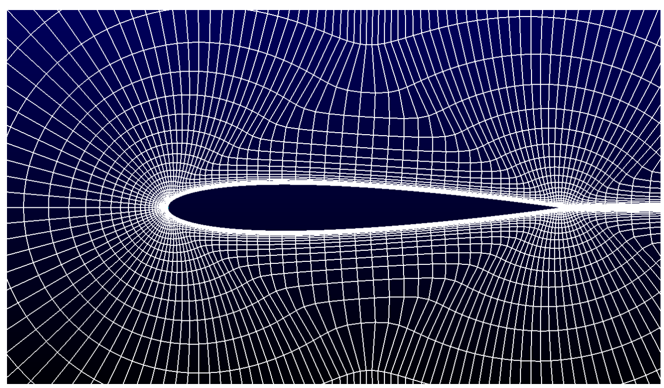

Figure 1. Zoomed mesh.

Perturbation	UQ_COMPONENT	UQ_PERMUTE
1c	1	NO
2c	2	NO
3c	3	NO
p1c1	1	YES
p1c2	2	YES

Table 2. Perturbation and corresponding setting options.

In Fig. 2, the parameter sweep study of C_L w.r.t. α obtained in this work is presented. The perturbed simulations are labeled

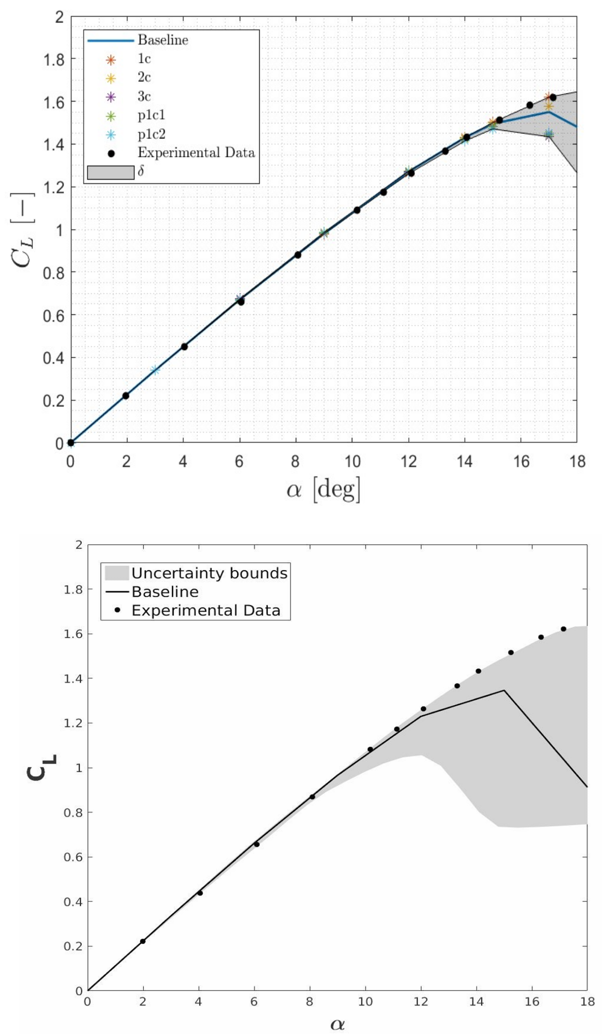

Figure 2. Parameter sweep analysis. Top: RANS prediction from this study against experimental data (Ref. 5). Bottom: RANS prediction from (Ref. 3).

according to the legend in Tab. 2. At low α, there is almost no difference ($\delta \approx 0$) between the perturbed RANS models, which in all cases fairly match the experiment. Closer to stall, for $\alpha \approx 16^\circ$, predictions from the baseline turbulence closure suffer a discrepancy w.r.t. the experimental data. In this region, the estimated uncertainty bounds are not negligible and, interestingly, include the experiment. In particular, perturbations *1C* and *2C*, which maximize the production term of TKE, exhibit higher values of C_L compared to the other simulations.

However, the results obtained in this thesis differ from the numerical results reported in (Ref. 3), see Fig. 2 on the bottom. The difference is very appreciable at high AOAs, revealing an inconsistency for $\alpha \geq 8^\circ$. This applies to both the baseline prediction and the uncertainty bounds estimate [1]. The reason was investigated and the root cause was found in an update of the SST turbulence closure occurred in the SU2 *8.0.0 Harrier* release, bearing in mind that results of (Ref. 3) were obtained using version *6.2.0 Falcon*.

[1]Note that, in Fig. 2 on the bottom, δ is indicated as *Uncertainty bounds*.

RESULTS

This study focuses on the application of uncertainty assessment to dynamic stall case studies, employing a coherence-based approach as proposed by G. Gori, O. P. Le Maître and P. M.Congedo (Ref. 4).

The dynamic stall is one of the major research topics in aeronautics, hydrodynamics and wind engineering (Ref. 6). An applicability of dynamic stall is in helicopter rotors during forward flight.

Two different case studies are considered:

- DeepDS: Deep dynamic stall of an OA 209 airfoil.
- LightDS: Light dynamic stall of NACA 23012 airfoil.

As previously said, dynamic stall is widely known in helicopters: during forward flight, the composition of forward and rotational speeds leads to significant differences between the local velocities over the rotor blades. Particularly, there is an increase in local velocity on the advancing blade and a decrease in velocity on the retreating blade. This introduces an imbalance in the rotor, often referred to as ”out-of-trim” condition. To address this imbalance, rotor trimming is achieved through the application of cyclic pitch. Specifically, the rotor blade is pitched up when the local velocity is low and pitched down when it is high. As a result, dynamic stall occurs. Due to the kinematics of the pitch rate reducing the adverse pressure gradient, the effective stall angle is larger than the static one for the retreating blade. Eventually, a delayed separation occurs and a vortex is formed and released, resulting in stall. This mechanism occurs as the blades rotate, entailing a strong time-dependence. Moreover, the blade also experiences the combined motions of pitching, flapping, cyclic pitch input, and wake-inflow effects.

LightDS occurs when the maximum AoA reached during the pitching cycle slightly exceeds the static stall angle, and is characterized by minor separation, small load deviations, and small hysteresis; DeepDS arises instead when the mean AoA is close to the static stall AoA of the airfoil, with a notably large oscillation amplitude ($\geq 5^\circ$) (Ref. 7). It is dominated by vortex-shedding phenomenon, large load deviations, and large hysteresis.

Pitching OA 209

Problem Setup We first consider the pitching OA 209, in two dimensions, subject to a DeepDS regime. Flow conditions are summarized in Tab. 3. The airfoil chord $c = 0.3\,\text{m}$ matches the wind tunnel tests from Gardner et al. (Ref. 8) and serves as the reference length in computing the aerodynamic coefficients.

Parameter	Value
Freestream Temperature	316 K
Freestream Mach Number	0.3
Reynolds Number	1.15×10^6
Reynolds Length	0.3 m

Table 3. Simulation parameters used for the analysis from (Ref. 8).

The freestream turbulence to laminar viscosity ratio ν_T/ν equals 4, according to the numerical investigation conducted by Wang et al. (Ref. 9). The turbulence intensity is set to 0.01, selected according to the best practice for high-quality flow within a wind tunnel test chamber.

URANS simulations rely on the K$-\omega$ SST turbulence model, which is also the baseline closure for the EQUiPS module. Furthermore, this model is preferred over the Spalart-Allmaras model (employed instead in (Ref. 8)) because it possibly offers a more detailed and robust representation of separated turbulent flows. In contrast, the Spalart-Allmaras model is well suited for predicting attached flows rather than complex dynamic stall phenomena.

Concerning the set up of the numerical solver. We select the Flexible Generalized Minimal Residual (FGMRES) method with an ILU (Incomplete Lower Upper factorization with connectivity-based sparse pattern) preconditioner to solve the linear system. The maximum number of linear iterations is set at 25 and the error threshold for its convergence is set at 1e$-$6. Although ILU has a higher computational cost compared to other preconditioners available in SU2 (Ref. 10), it offers superior effectiveness in accelerating convergence. An Euler implicit time discretization scheme is used. The convective fluxes are computed using an upwind method of Roe type. To achieve second order accuracy in space, the Monotonic Upwind Scheme for Conservation Laws (MUSCL) reconstruction is adopted. The Venkatakrishnan slope limiter is employed to attenuate the solution oscillations in regions with steep gradients. The convergence criterion targets the density root mean square, imposing a threshold value to 1e$-$6.

A second-order implicit dual-time-stepping integration scheme is used, with a time step fixed at 1.09×10^{-4} s. Each time-step includes 50 inner iterations and the maximum physical time is set to 0.57 s. A choice that allows for a more precise capture of unsteady behavior and ensures that significant flow dynamics are not neglected. After an iterative process, the CFL number is set to 5.

Mesh definition Preliminary RANS simulations are performed to assess farfield independence and mesh convergence. An adapted CFL number is effective for steady simulations. The convergence criterion targets the density root mean square, requiring a value below the 1e$-$9 threshold. The mesh is a structured O-grid, chosen for its suitability in capturing the varying flow fields associated with dynamic stall. To improve computational efficiency and avoid unnecessary detail in less critical regions, the point spacing along the airfoil is not uniform: cells are finer closer to the leading and the trailing edges. The number of points on the central upper surface is set equal to the number of points on the central lower surface. The resulting mesh is shown in Fig. 3, with details exposed in Fig. 4 and Fig. 5. Note that the trailing edge is rounded to improve cell extrusion in a region crucial for simulations.

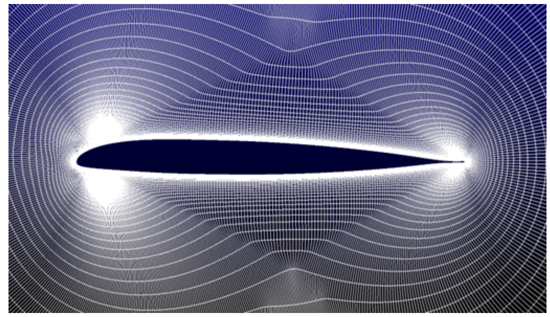

Figure 3. Overall mesh.

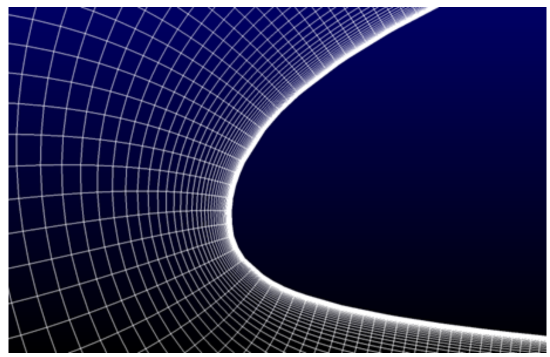

Figure 4. Leading edge zoom.

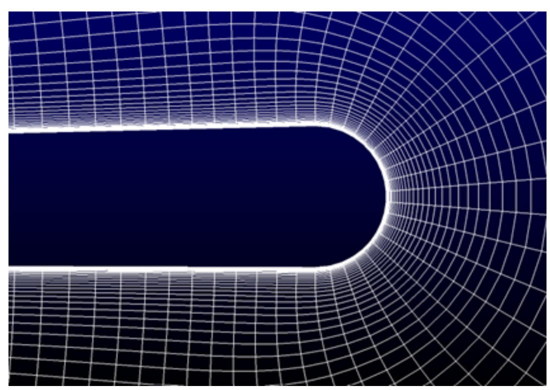

Figure 5. Trailing edge zoom.

In all meshes, the height of the first cell is chosen to ensure that $y^+ \leq 1$, allowing for proper resolution of the flow near the wall and providing accurate results.

Space and time independence assessment are described below.

It must be said that one should perform these two independence processes both for baseline and perturbed simulations, as each perturbation leads to a different realization of the Reynolds stress tensor which, ultimately, implements a different physics. As reported in (Ref. 4), one should not expect the six cases to exhibit the same grid and time resolution dependency. However, proving convergence w.r.t. the baseline model is deemed sufficient. Possible issues related to perturbed simulations are anyway going to be collected in the uncertainty estimates. The consequence is that uncertainty estimation will not only be related to purely physical aspects, but also to numerical ones (grid related). Thus, the analysis reported in the following is performed considering the baseline grid only; this choice is simpler and computationally effective.

To save computational resources, we assess the farfield independence considering the steady blade and only for $\alpha = 13°$. The radius r of the O-grid is systematically increased, with each subsequent grid doubling the radius, starting from $r = 30 \times c$ up to $r = 120 \times c$.

Table 4 reports the characteristics of each grid i.e., radius (**r**), size as number of points on the airfoil times the number of points in the radial direction, the total number of cells, the value of C_L at AoA equal to 13°, and the correspondent percentage variation w.r.t. the previous mesh.

Domain	**r [m]**	**Size**	**N Cells**	C_L	Δ_{C_L} **[%]**
30 c	9	357×63	22,072	1.396	-
60 c	18	357×66	23,140	1.393	-0.22%
120 c	36	357×69	24,208	1.392	-0.09%

Table 4. Farfield independence mesh parameters.

The choice is conservative compared to the dimensions used in (Ref. 15), where an O-grid with $r = 50 \times c$ is employed.

To save computational resources, also mesh convergence is assessed considering the steady blade and only for $\alpha = 13°$. The number of points on the airfoil is systematically increased by approximately 35% and the growth rate is reduced by 5% with each subsequent mesh, starting from the coarse mesh, which is characterized by 368 points on the airfoil and a growth rate of 1.2.

Table 5 reports the characteristics of each grid i.e., size as number of points on the airfoil times the number of points in the radial direction, the total number of cells, the value of C_L at AoA equal to 13°, and the correspondent percentage variation w.r.t. the previous mesh. The relative error between the

Domain	**Size**	**N Cells**	C_L	Δ_{C_L} **[%]**
Coarse	357×69	24,208	1.392	-
Coarse-Medium	477×84	39,508	1.426	2.46%
Medium	617×107	65,296	1.452	1.77%
Fine	917×186	169,460	1.458	0.42%

Table 5. Grid convergence mesh parameters.

Medium mesh and the *Coarse-Medium* one is 1,77%, while the error between the *Fine* mesh and the *Medium* is 0,42%. The selected domain is the *Medium* one, as it offers the best compromise between detail and computational cost.

Time Convergence To account for the pitching motion of the airfoil URANS simulation are performed, using a Mach number $M = 0.3$ and a rigid rotation of mesh around the angle $\alpha_0 = 13°$ with frequency $f = 5.7\,\text{Hz}$ (reduced frequency $\omega^* = 0.11$, $\omega^* = 2 \cdot \pi \cdot \frac{f}{u}$) and amplitude of 7°. The airfoil AoA α is computed from Eq. 7, where $\Omega = -2\pi f$, $N_{t_{iter}}$ is the current time iteration and Δt is the time step.

$$\alpha = \alpha_0 + 7° \cdot \sin\left(\Omega N_{t_{iter}} \Delta t\right), \tag{6}$$

To initialize the problem, one quarter of cycle is performed from the angle α_0, then three full cycles are simulated.

It is essential to ensure a time step sufficiently small to accurately capture the unsteady phenomena. Accordingly, three different time steps are considered, each obtained dividing the period of the pitching oscillation by the number of time steps per cycle.

- Coarse time step: 800 iterations per cycle ($\Delta t = 2.19 \times 10^{-4}$ s);
- Medium time step: 1600 iterations per cycle ($\Delta t = 1.09 \times 10^{-4}$ s);
- Fine time step: 3200 iterations per cycle ($\Delta t = 0.55 \times 10^{-4}$ s).

Fig. 6 compares the C_L histories predicted using the different time steps.

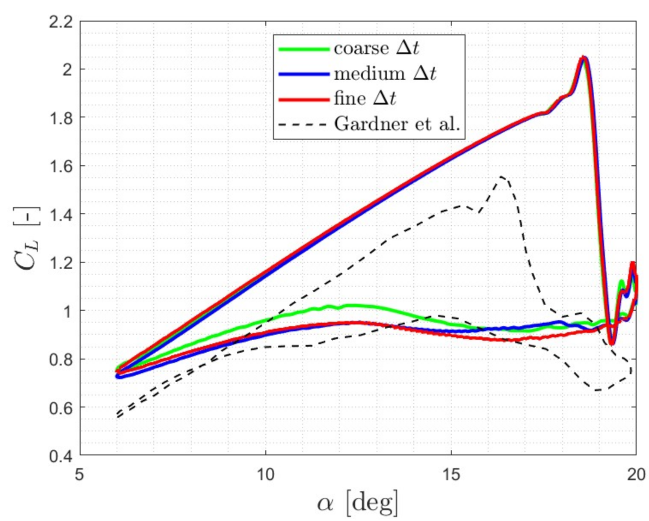

Figure 6. Time convergence of average C_L.

All time steps lead to a similar prediction of the C_L peak during the pitch up of the blade (upper portion of the curve). Quantitatively, the difference in peak magnitude between the *medium* and the *coarse* time steps is 0.49%, whereas the difference between the *fine* and *medium* simulations is also 0.49%. The α at which the peak is estimated is 18.56° for the *coarse* case, 18.59° for the *medium* simulation and 18.57° for the *fine* one. However, the curve differs from the reference of

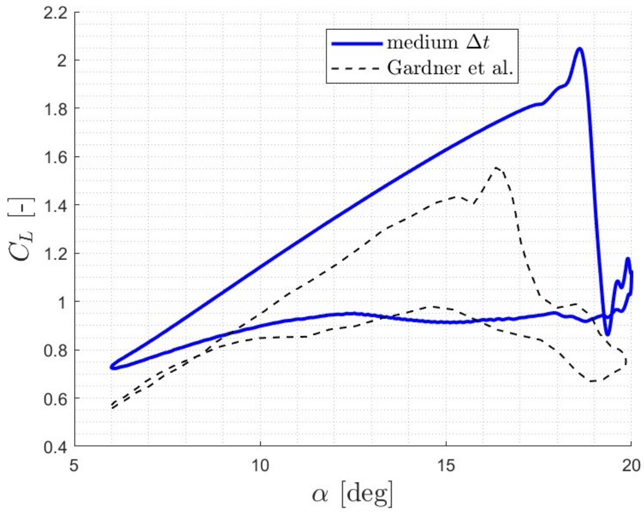

Figure 7. Average C_L of the selected time step.

A. D. Gardner, K. Richter, H. Mai and D. Neuhaus (Ref. 8) due to a shift of the peak value towards higher AoA and C_L values as shown in Fig. 6.

CFD performed by K. Richter, A. Pape, T. Knopp, M. Costes, V. Gleize and A. Gardner (Ref. 17) of the same case, but conducted by using ONERA aerodynamic code elsA and with a finer mesh, shows similar results (see *"elsA-SST-fully turbulent"* against *"TWG-DS2"* in Fig. 8): the C_L peak is 10% higher and the AoA at which the peak is reached is 0.2° higher compared to the values obtained with *SU2*.

Observing the pitch down phase in Fig. 6, one could notice a stronger similarity between the *fine* and *medium* time steps compared to that between the *medium* and *coarse* time steps. Also in this case, each simulation provides different results compared to the reference. The same behavior is observed in Fig. 8, where the simulation *"elsA-SST-fully turbulent"* shows significant differences from the experiments *"TWG-DS2"*.

According to the analysis, the *medium* time step is selected (see Fig. 7).

Baseline flow analysis We now investigate the unsteady flow predicted using the baseline SST turbulence closure. From Fig. 9 to Fig. 14 we report the Mach number distribution of the flow field at different AoA, along with the visualization of the streamlines.

Please note that to simulate the pitching motion the airfoil has been rotated of ±7°, while the airflow has an inclination of 13°. (i.e. 6° during pitch down phase is obtained with the airfoil rotated of −7°)

From Fig. 9 to Fig. 14 one could notice a typical flow behavior in dynamic stall, as described by W. C. Lawrence, K. W. McAlister and W. J. McCroskey (Ref. 16). At first, in Fig. 9, the flow is fully attached. Then, during pitching motion Fig. 9 to Fig. 10 the airfoil passes the static angle of attack, where there are no detectable changes in the flow. At higher AoA (Fig. 11) there is a Dynamic Stall Vortex (DSV) formation at

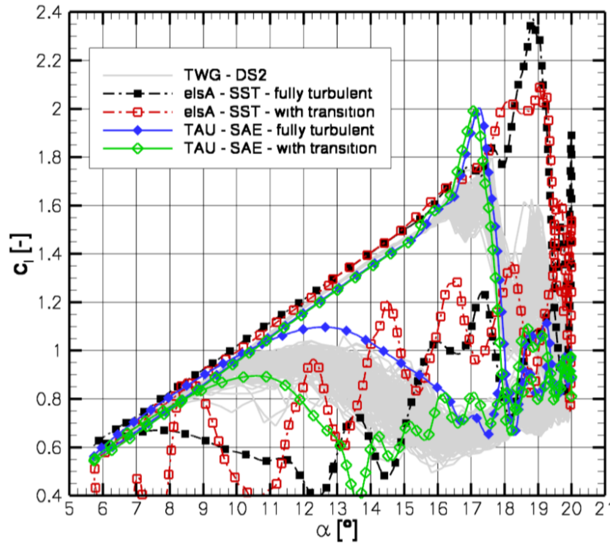

Figure 8. Average C_L from the analysis conducted with code elsA in (Ref. 17).

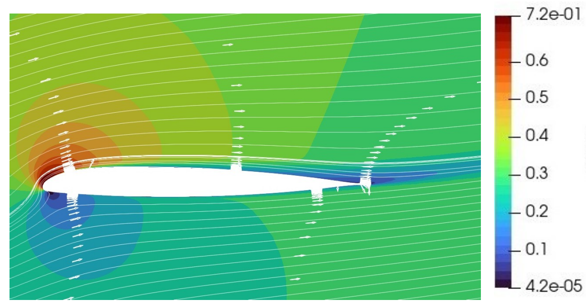

Figure 9. Pitch up 9.9°.

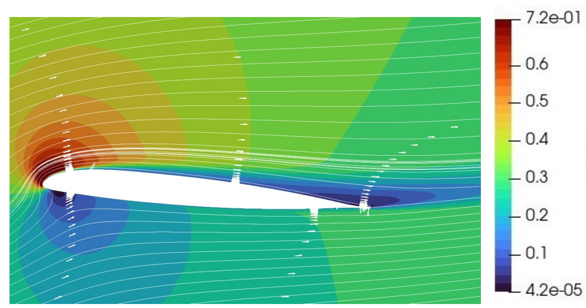

Figure 10. Pitch up 17.5°.

the leading edge, according to Lawrence et al. (Ref. 16), this situation is characterized by the beginning of moment C_m stall (see point *b* in Fig. 16). As reported in (Ref. 16), the DSV formation process is also characterized by an increase in the slope of lift curve, point *c* in Fig. 15.

DSV is followed by the Shear Layer Vortex (SLV) which is subsequently shed at trailing edge (Fig. 12). This condition corresponds to the local minimum of C_L depicted in Fig. 7, while there are no significant changes in C_m at AoA between 19.2° and 20°. In the second half of the pitching oscillation,

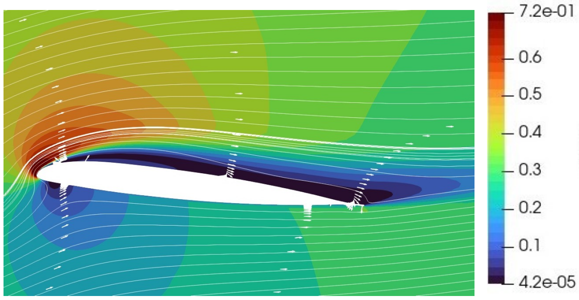

Figure 11. Pitch up 18.6°**.**

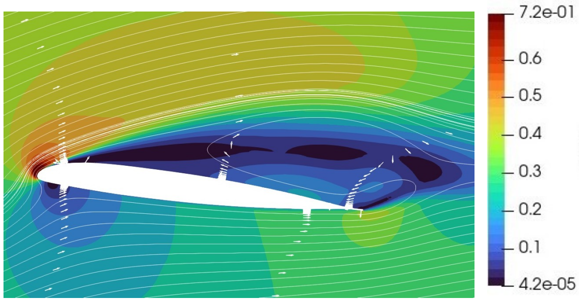

Figure 12. Pitch up 19.2°**.**

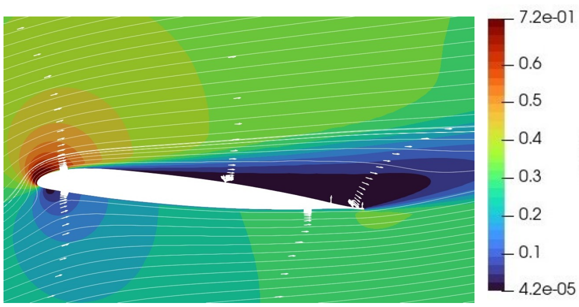

Figure 13. Pitch down 17.1°**.**

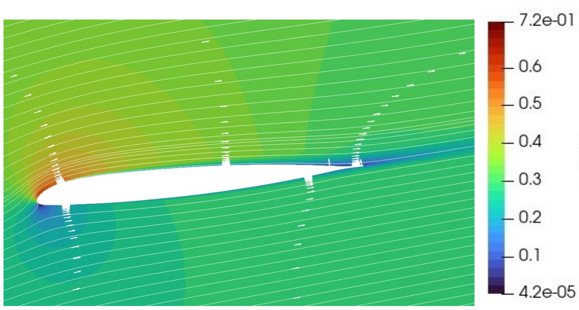

Figure 14. Pitch down 6.5°**.**

one could observe the reattachment of the boundary layer: the flow reattaches progressively from the leading edge (Fig. 13). Then a full reattachment occurs before the minimum angle is reached (Fig. 14).

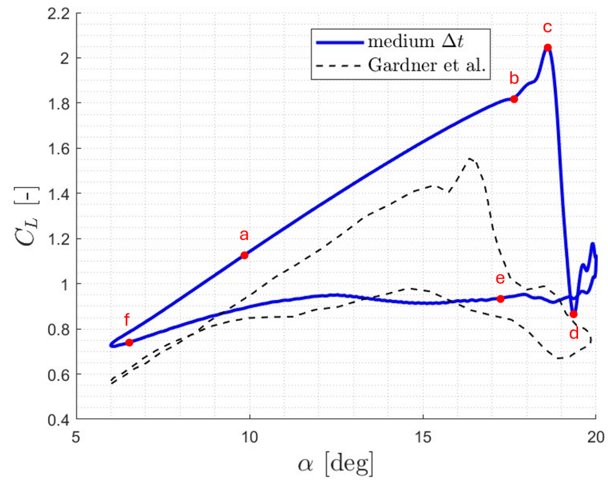

Figure 15. Average C_L of the selected time step. Dotted mark in figure is associated to the flow configuration reported from Fig. 9 to Fig. 14.

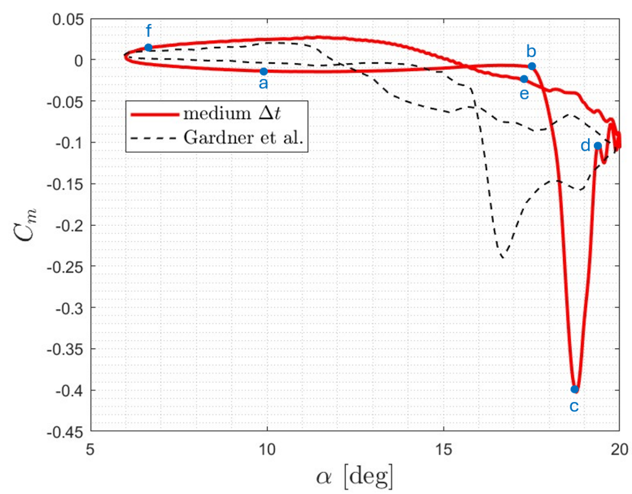

Figure 16. Average C_m for the selected time step. Dotted mark in figure is associated to the flow configuration reported from Fig. 9 to Fig. 14.

Uncertainty Analysis We apply the EPM to assess the credibility of unsteady RANS predictions. Figure 17 depicts the baseline CFD prediction of C_L and the five perturbed ones, and compare them against the reference (Ref. 8), while Fig. 18 shows results in terms of C_m obtained from the six simulations against the reference (Ref. 8).

Considering the C_L predictions in Fig. 17, during the pitch up phase, a good agreement between six simulations is shown, while during the pitch down phase an high discrepancy could be observed.

As one could notice, looking at C_m, simulations seem to provide similar results and close to the reference in the pitching up motion until 14° and up to 12° during the pitch down (Fig. 18). It should be also mentioned that C_m simulations appear to provide a stronger agreement during the pitch down phase, compared to the C_L predictions.

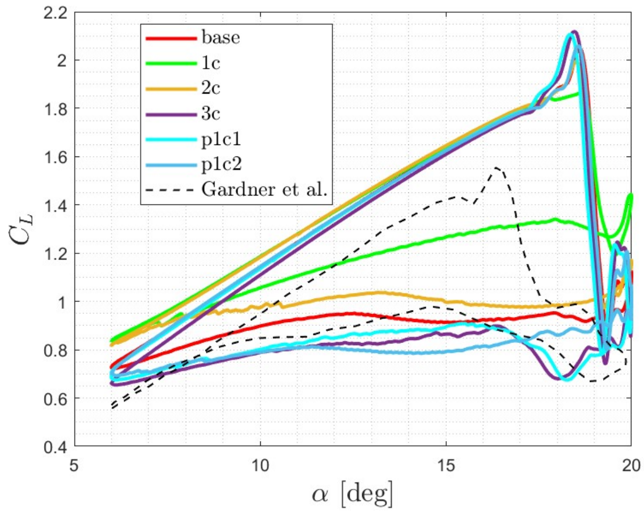

Figure 17. Average C_L perturbed simulations.

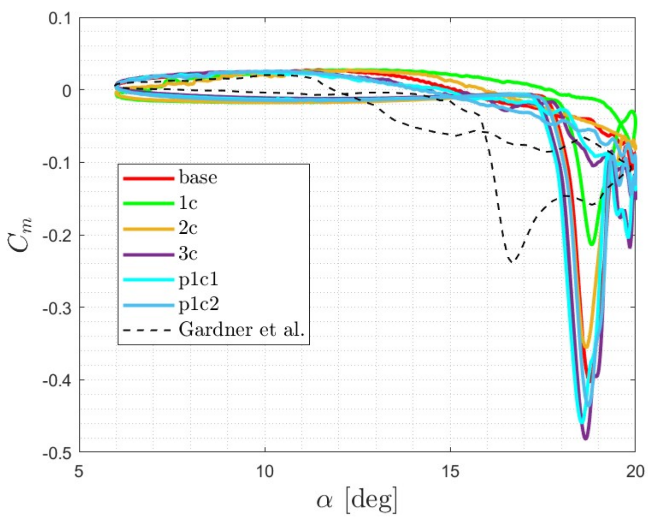

Figure 18. Average C_m perturbed simulations.

The discrepancy between simulations and experimental results during the pitch-down motion can be attributed to the fact that URANS simulations are inherently limited when addressing complex phenomena such as dynamic stall. One could be surprised by the different behavior of C_L and C_m during the pitch-down phase. While the lift coefficient C_L shows significant discrepancies between perturbations, the moment coefficient C_m appears to yield roughly similar results across the six simulations. In particular, during pitch-down at 12°, C_L exhibits a wide spread, whereas C_m results are gathered around similar values. For this latter, during the pitch-down phase, the perturbations display notably different results. In particular, the *1C* simulation provides a C_m that is 47% higher than that of the *p1c1* simulation. On the contrary, predictions are closer during the pitch up.

Figure 19 and Fig. 20 show C_p distribution over the airfoil at $\alpha = 12^\circ$ for both the pitch down and up phases, respectively. For the first, it can be noticed that the C_p distributions

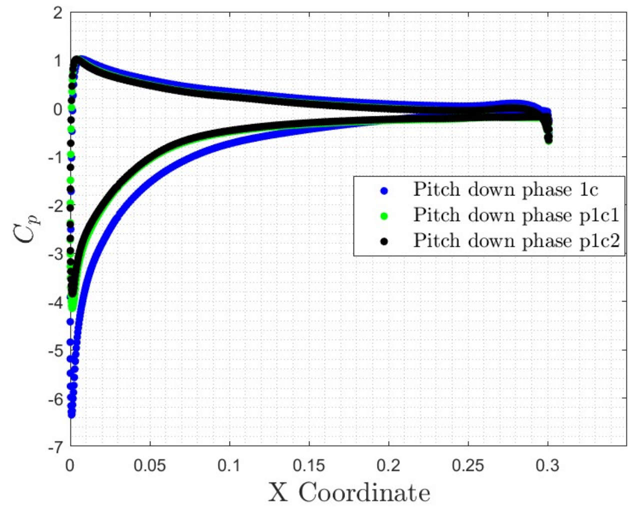

Figure 19. C_p distribution over the airfoil at 12° during the pitch down phase.

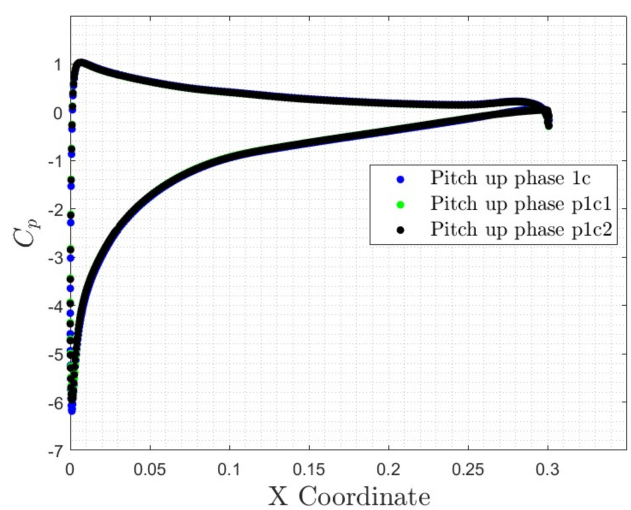

Figure 20. C_p distribution over the airfoil at 12° during the pitch up phase.

with larger areas are associated with perturbations yielding higher C_L values. The *1C* simulation (the one maximizing the production term of TKE) shows the largest peak, while *p1c2* exhibits the lowest. One could also observe that the C_p distribution of *1C* is the most front-loaded, resulting in the highest value of C_m.

Although the pitch down phase shows significant differences among simulations, the pitch up phase exhibits agreement. This indicates that during the pitch up phase, simulations are less sensitive to the perturbation applied. In this case, the discrepancies between reference data and simulations are possibly not attributable to the uncertainty of the turbulence closure. We stress that this is not a strong conclusion since the EQUiPS implementation of the EPM is not fully agnostic w.r.t. the baseline closure i.e., the SST model. In fact, the turbulent kinetic energy factor is not perturbed, forcing a certain dependency on the baseline closure. To generalize the statement, further investigations could be conducted using the Spalart-Allmaras closure as the baseline.

Since the EQUiPS module perturbs the eigenvector alignment to modulate the TKE production term $\mathscr{P}$, it was decided to target the turbulent kinetic energy (TKE) as one quantity of interest. Note that the quantity of interest is actually the TKE integrated over a closed line circling the airfoil. Although this integration provides a global measure, it also introduces a potential limitation due to the loss of local information that might be critical for understanding flow dynamics. However, compared to C_L and C_m, the integrated TKE remains more sensitive to turbulence-related processes. To mitigate the potential loss of local information, after a sensitive analysis, it was decided to consider a circle area with radius $r = 2\,\text{m}$.

We analyze the power spectral density (PSD) and coherence of TKE signals as produced by the different EPM simulations. Note that, according to the Nyquist–Shannon sampling theorem, the selected time step allows to correctly sample frequencies up to 4559 Hz. The PSD of the baseline signal is reported in Fig. 21. Surprisingly, perturbed EPM simulations return very similar spectra in the range 0-15 Hz. Above 15 Hz, slight differences can be found, but the energy content is so small to render such differences negligible. Given the magnitude of the perturbations applied, stronger differences were somehow expected among the six simulations.

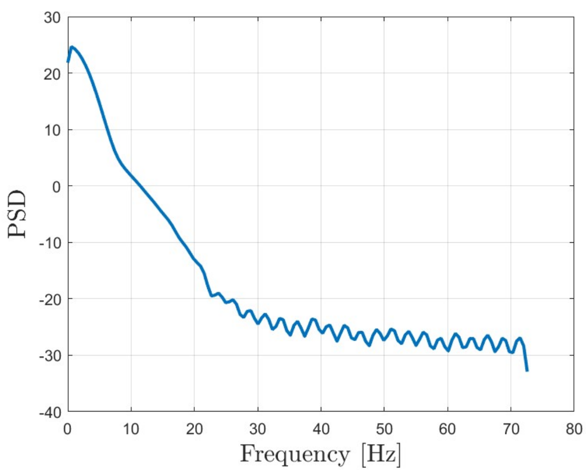

Figure 21. PSD of the integrated TKE for baseline simulation.

Figure 22 shows the averaged coherence among the signals (since coherence is a function of frequency it was decided to report the average of it). As one could notice, the highest coherence (close to 0.9) is between *1C* and *2C*, the perturbations that maximize TKE production. As expected, signals *p1c1* and *p1c2*, which represent the Reynolds tensor realization that minimize the production of TKE, do not show high coherence with *1C* and *2C*. However, it must be said that the PSD peak is expected at 5.7 Hz, since the phenomenon studied is governed by the airfoil motion frequency, while the actual peak

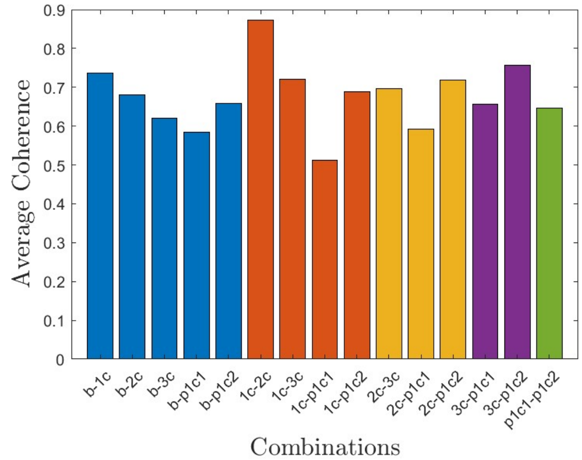

Figure 22. Averaged coherence of the integrated TKE signals between all simulations.

is highlighted at a lower frequency. For this reason, leakage and scalloping were investigated to assess if the selected window would be able to prevent the spread of PSD signal among frequencies and the reduction of amplitude of the signal itself.

The plots are not reported for conciseness. Indeed, the windowing provides a higher coherence compared to the *unwindowed* case, but it is not meaningful. Thanks to the windowing, additional peaks are now captured; however, the main peaks are still far from the main interest frequency 5.7 Hz. This could be due to the choice of analyzing the integrated TKE over a portion of the domain, resulting in a loss of important local information which is not sufficiently captured.

An analysis of PSD and coherence is also performed considering the C_L and C_m signals, with Hann windowing. Again, spectra are very similar thus we report only the one associated to the baseline prediction of C_L, Fig. 23, and C_m, Fig. 24.

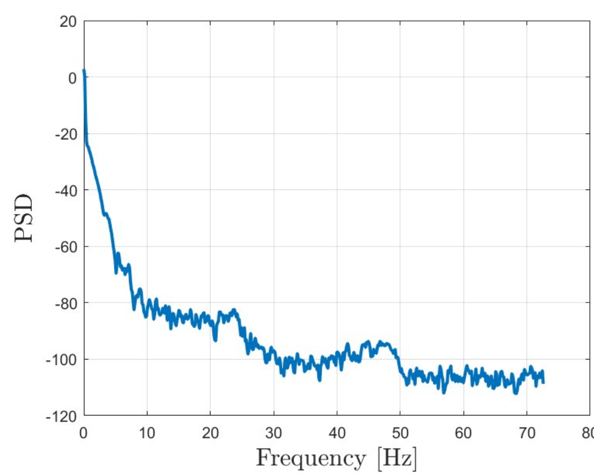

Figure 23. C_L PSD of the baseline simulation with Hann windowing.

The PSD of the coefficients produces results different from the TKE. However, the main peak is still located a low fre-

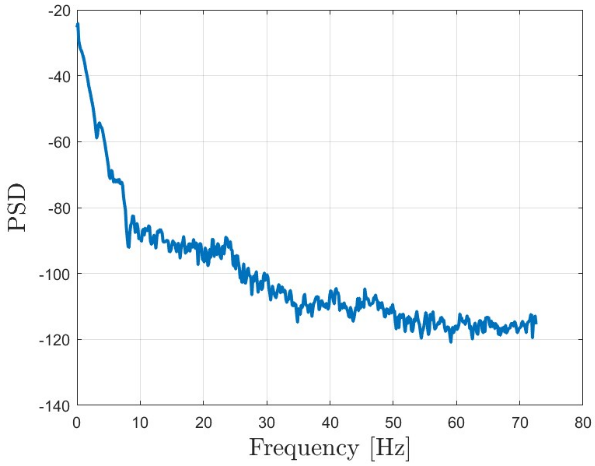

Figure 24. C_m PSD of the baseline simulation with Hann windowing.

quencies ($\leq 5.7\,\text{Hz}$), as obtained in the TKE approach. This means that the main frequency is not captured as expected, even if a different quantity is targeted is used. Figure 25 and Fig. 26 report the average coherence between, respectively, the C_L and C_m signals. It can be noticed that these are significantly lower than the ones obtained for the integrated TKE, being the reported values generally ≤ 0.3. According to this, the URANS predictions are highly sensitive to perturbation of the turbulence closure, suggesting a poor credibility and the need of a higher-fidelity approach.

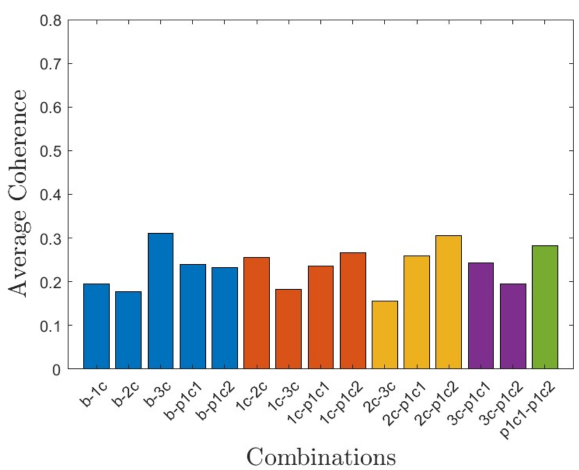

Figure 25. Averaged coherence of C_L between all the simulations with Hann windowing (coefficient approach).

Pitching NACA 23012

Problem Setup We show now the pitching NACA 23012, in two dimensions, subject to a LightDS regime. This test case refers to the work of Zanotti (Ref. 7). Flow conditions are summarized in Tab. 6. The airfoil chord is the same as used

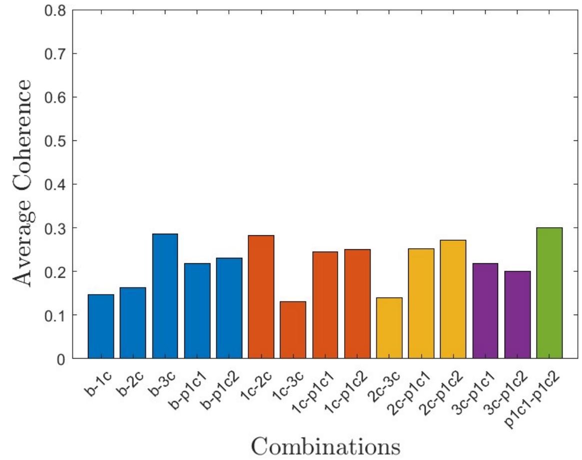

Figure 26. Averaged coherence of C_m between all the simulations with Hann windowing (coefficient approach).

in Ref. (Ref. 7); the reference length, used to compute the aerodynamic coefficients, is taken equal to the chord c.

Parameter	Value
Freestream Temperature	299 K
Freestream Mach Number	0.15
Reynolds Number	1.0×10^6
Reynolds Length	0.3 m

Table 6. Simulation parameters used for the analysis from (Ref. 7).

The setup of the CFD URANS solver is the used in Sec. *RESULTS - Pitching OA 209 - Problem Setup*. As primary study it was decided to adopt a simple O-grid type mesh with the same dimensions and resolution adopted by Zanotti (Ref. 7), as it provides an optimal compromise between simplicity and agreement with experiments. The mesh is characterized by a farfield of 20 chord lengths; 600 points discretize the surface of the airfoil, with a first cell height selected to ensure $y^+ \leq 1$ to allow the proper resolution wall boundary layer. URANS simulations are performed considering a rigid mesh subject to harmonic rotation around $\alpha_0 = 5°$ with frequency $f = 5.5\,\text{Hz}$ and amplitude of $10°$.

$$\alpha = \alpha_0 + 10° \cdot \sin\left(\Omega N_{t_{iter}} \Delta t\right), \tag{7}$$

where $\Omega = -2\pi f$, $N_{t_{iter}}$ is the current time iteration, and Δt is the time step. To initialize the problem, one quarter of cycle is performed from the angle α_0, then three full cycles are simulated. Considering that the pitching frequency is similar to that of the DeepDS case study, the assumption is made that the number of iterations per period used for the OA 209 airfoil can be applied without conducting a time convergence study. Hence 1600 iterations per period are used, yielding a time step of $\Delta t = 1.13 \times 10^{-4}$ s which is very close to the value adopted for the OA 209 airfoil ($\Delta t = 1.09 \times 10^{-4}$ s).

A comparison between the reference (Ref. 7) and the computational results obtained in this thesis is shown in Fig. 27 and

Fig. 28. A certain shift from the experiment is present both in

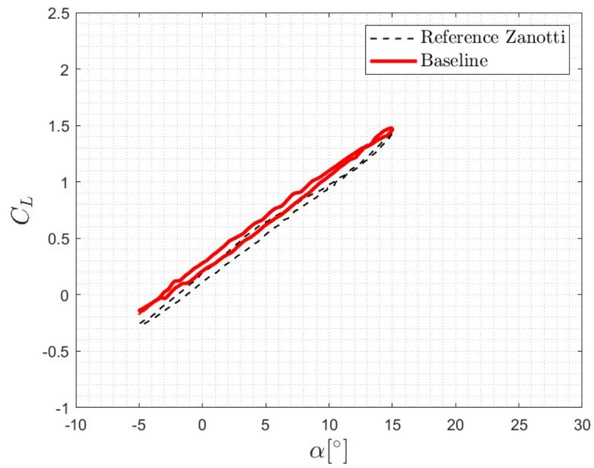

Figure 27. Average C_L from URANS simulations compared with experiments (Ref. 7).

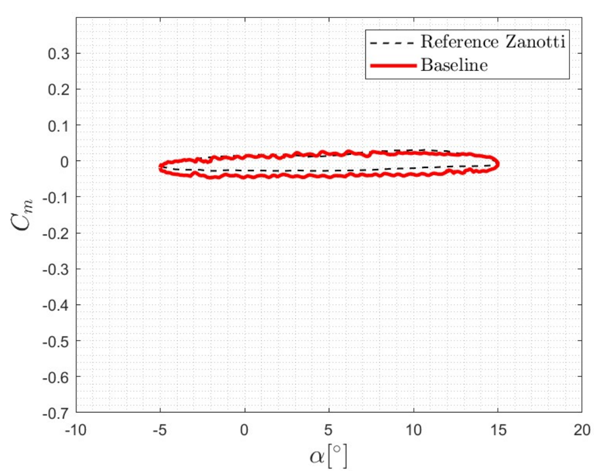

Figure 28. Average C_m from URANS simulations compared with experiments (Ref. 7).

C_L and C_m simulations. A source of discrepancies could be the boundary effect of the wind tunnel, which is not reproduced by a 2D URANS simulation.

Uncertainty analysis The EQUiPS module of *SU2* is employed to investigate the credibility of the turbulence model. Figure 29 and Fig. 30 report the baseline and the EPM perturbed predictions of C_L and C_m, respectively, and compare them with the reference (Ref. 7).

It is not surprising that, for a LightDS case study, all the EPM simulations return similar results. In Fig. 29, all the EPM predictions for the C_L coefficient exhibit a good agreement, confirming a poor dependency of the CFD model on the perturbations applied to the turbulence closure. This observation is valid for both the pitch-up and pitch-down phases. Overall,

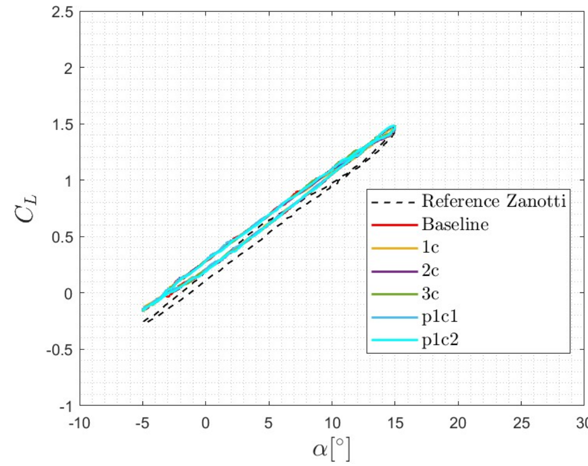

Figure 29. Average C_L for the baseline and perturbed URANS simulations compared with reference (Ref. 7).

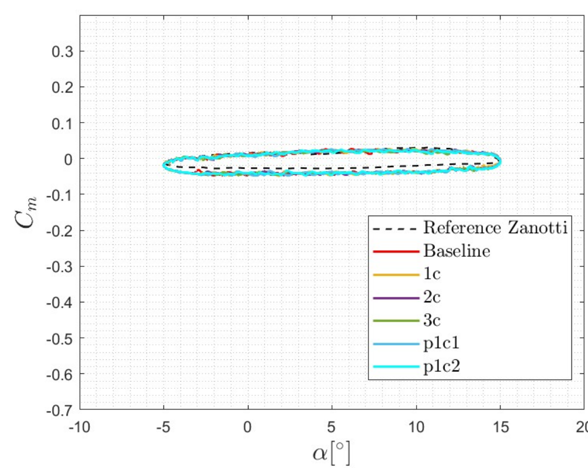

Figure 30. Average C_m for the baseline and perturbed URANS simulations compared with reference (Ref. 7).

an upward shift from the experiment values is appreciable. In Fig. 30, all C_m predictions are similar results and close to the reference in the pitching-up motion, until 10°. During the pitch-down, we find a discrepancy with respect to the experiment. However, all simulations are still very similar.

The PSD analysis of the integrated TKE is carried out similarly to the previous case. The TKE is integrated over a line circling the airfoil. Given the issues encountered for the previous test case, it was decided to consider a smaller circle with radius $r = 0.7\,\text{m}$. According to the Nyquist–Shannon sampling theorem, the selected time step allows sampling frequencies up to 4413.02 Hz. The PSD analysis is reported for the baseline signal only in Fig. 31, being all the EPM results similar. Given that a LightDS is investigated, an even higher similarity is expected compared to the OA209 case study. Consequently, the investigation of DeepDS through URANS simulations presents greater challenges compared to LightDS. DeepDS is primarily governed by vortex shedding, large load deviations, and pronounced hysteresis effects, which contribute to its increased complexity. On the contrary,

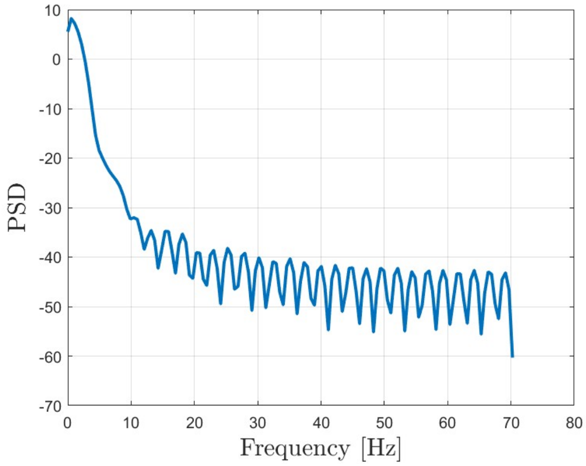

Figure 31. PSD of the integrated TKE for baseline simulation.

LightDS features more limited flow separation, smaller load deviations, and reduced hysteresis, leading to a less complex flow regime. Hence, results for LightDS are expected to exhibit higher consistency across the six simulations, as confirmed by our numerical experiments.

In Fig. 32, we report the averaged coherence. As expected,

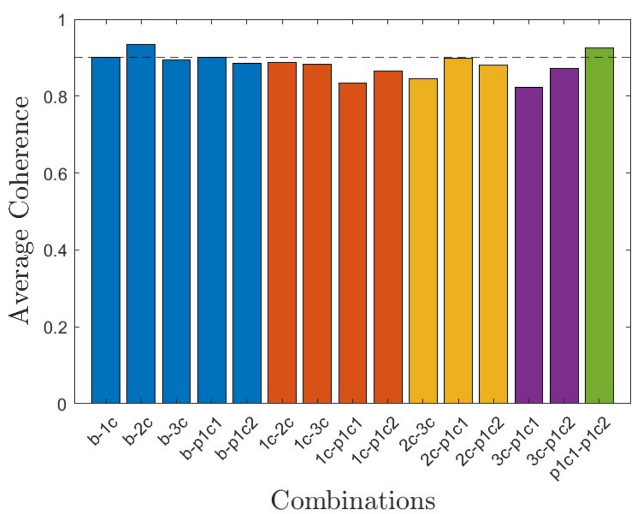

Figure 32. Averaged coherence between all the simulations (TKE approach).

averaged coherence is high for all possible combinations of signals ≥ 0.8. In particular, *p1c1* and *p1c2*, as well as *base* and *2C*, which show the highest value. Since the first two perturbations are characterized by the minimization of the TKE production term, these show a coherence value ≥ 0.9. A high credibility of the turbulence model for this case study is expected.

Perturbations associated with a lower TKE production yield very similar results in terms of both aerodynamic coefficients and energy metrics (TKE). This highlights that results remain consistent despite extreme perturbations of Reynolds stress tensor. Possibly, differences between experiments and simulations are not due to the epistemic uncertainty in the turbulence closure. However, it must be said that the PSD peak is expected at 5.5 Hz, since the phenomenon studied is governed by the airfoil motion frequency, while the actual peak is highlighted at a lower frequency. Also for this case we assessed if the selected window would be able to prevent the spread of PSD signal among frequencies and the reduction of amplitude of the signal itself. Hann windowing was applied, as was done for the OA209 analysis, but differences in PSDs are not relevant.

The main peak is still far from what expected frequency.

Similarly to the previous case, the PSD and coherence analyses are performed considering C_L and C_m. Figure 33 and Fig. 34 report such analyses for the baseline prediction only since perturbed simulations returns similar results.

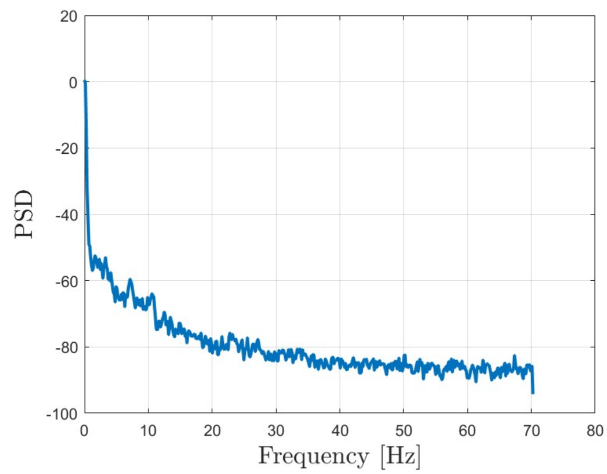

Figure 33. C_L PSD of the baseline simulation with Hann windowing.

Figure 35 and Fig. 36 show the average coherence values.

The average coherence values are shown in Fig. 35 (C_L) and Fig. 36 (C_L), and exhibit lower coherence values compared to the analysis targeting the integrated TKE. For both coefficients C_L and C_m, the coherence values range between 0.5 and 0.7. However, it must be said that compared to the same analyses performed for the DeepDS case, Fig. 25 and Fig. 26, the coherence is significantly higher. Not surprisingly, this suggests that the LightDS case is less sensitive to the turbulence closure compared to the DeepDS one. For sure, there is a difference between experiments and computations which can be attributed to boundary effects (which cannot be captured with a 2D URANS simulation) and to the complexity of reproducing a the dynamic stall phenomenon using a 2D approximation.

For future studies an higher-fidelity simulation would be useful to confirm that, for the LightDS case study, a saving of computational effort is possible using URANS with EQUiPS

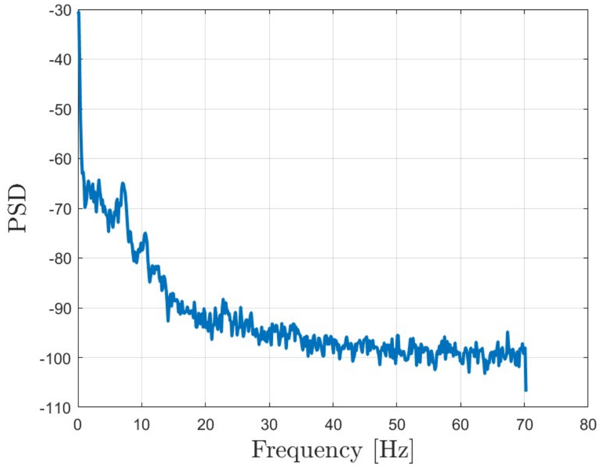

Figure 34. C_m PSD of the baseline simulation with Hann windowing.

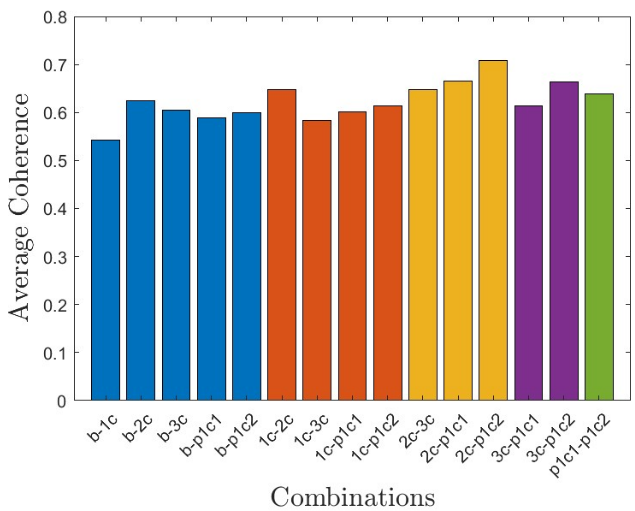

Figure 35. Averaged coherence of C_L between all the simulations with Hann windowing (coefficient approach).

module and the fidelity assessment procedure described before.

CONCLUSIONS

URANS simulations are subject to epistemic uncertainty related to the turbulence closure. A key research objective is the credibility assessment of these simulations, determining whether URANS can be considered reliable to address a research question. In rotorcraft applications, the level of uncertainty arises because simulations generally target the analysis of complex unsteady phenomena e.g., dynamic stall.

To address the issue of evaluating the credibility of URANS for such applications, we explored the use of the Eigenspace Perturbation Method (EPM) implemented via the EQUiPS module in the SU2 solver. The EPM is a valuable tool to predict uncertainty in steady cases, but rarely are applications found for the unsteady ones. For these latter, estimating the

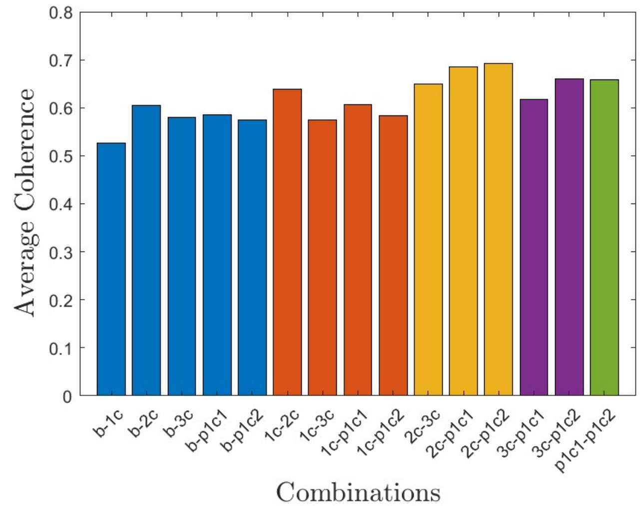

Figure 36. Averaged coherence of C_m between all the simulations with Hann windowing (coefficient approach).

uncertainty bound using the max-min difference (δ) is not adequate due to the possibly different harmonic content and phase shift of the time series. Therefore, to assess credibility of URANS simulations, we explored the use of diverse approaches. Namely, PSD and coherence among signals produced by the baseline and the 5 EPM simulations.

Two test cases are evaluated. These are representative of deep and light dynamic stall conditions for rotorcraft blades. For the OA209, results suggest a high sensitivity of URANS predictions to the turbulence closure. In fact, the epistemic uncertainty inherent in the closure questions the credibility of predictions with particular reference to the pitch down phase. During the pitch down, a large dispersion is observed among the six simulations, whereas predictions are not that different in the pitch up. On the contrary, for the light dynamic stall case a low sensitivity to the perturbation of the turbulence closure is observed. Namely, all EPM predictions, including the baseline one, show a good agreement in both the pitch up and pitch down phases. However, a shift is recorded with respect to the reference data which may be attributed to the many approximations underlying the CFD model e.g., 2D approximation.

Future studies could consider quantities of interest different than the ones targeted in this paper, with possibly a special focus on geometric features critical to design and performance e.g., the leading edge.

Author contact:
Federico Vegetti federico.vegetti@leonardocompany.com
Giulio Gori giulio.gori@polimi.it

ACKNOWLEDGMENTS

This work was funded by the European Union (Project 101059320 - UN-BIASED). Views and opinions expressed are however those of the author(s) only and do not necessarily reflect those of the European Union or the European Research

Executive Agency. Neither the European Union nor the European Research Executive Agency can be held responsible for them.

REFERENCES

1. T. D. Economon, F. Palacios, S. R. Copeland, T. W. Lukaczyk, and J. J. Alonso, "SU2: An open-source suite for multiphysics simulation and design," *AIAA Journal*, vol. 54, no. 3, pp. 828–846, 2016.

2. G. Iaccarino, A. A. Mishra, and S. Ghili, "Eigenspace perturbations for uncertainty estimation of single-point turbulence closures," *Phys. Rev. Fluids*, vol. 2, no. 2, p. 024605, Feb. 2017.

3. A. A. Mishra, J. Mukhopadhaya, G. Iaccarino, and J. Alonso, "Uncertainty estimation module for turbulence model predictions in SU2," *AIAA Journal*, vol. 57, no. 3, pp. 1066–1077, 2019.

4. G. Gori, O. P. Le Maître, and P. M. Congedo, "On the sensitivity of structural turbulence uncertainty estimates to time and space resolution," *Computers & Fluids*, vol. 229, p. 105081, 2021.

5. C. Ladson, "Effects of independent variation of Mach and Reynolds numbers on the low-speed aerodynamic characteristics of the NACA 0012 airfoil section," NASA Technical Memorandum 4074, Langley Research Center, 1988.

6. W. J. McCroskey, "The Phenomenon of Dynamic Stall," NASA Technical Memorandum 81264, 1981.

7. A. Zanotti, "Retreating Blade Dynamic Stall," Ph.D. dissertation, Politecnico di Milano, 2012.

8. A. D. Gardner, K. Richter, H. Mai, and D. Neuhaus, "Experimental control of compressible OA209 dynamic stall by air jets," *Journal of the American Helicopter Society*, vol. 59, no. 2, pp. 1–11, 2012.

9. S. Wang, L. Ma, D. B. Ingham, M. Pourkashanian, and Z. Tao, "Turbulence Modelling of Deep Dynamic Stall at Low Reynolds Number," in *Proc. World Congress on Engineering*, vol. II, London, U.K., 2010.

10. SU2 Developers, "Linear Solvers and Preconditioners — SU2 Documentation," 2024. [Online]. Available: https://su2code.github.io/docs_v7/Linear-Solvers-and-Preconditioners

11. J. Ling and J. Templeton, "Evaluation of machine learning algorithms for prediction of regions of high Reynolds averaged Navier–Stokes uncertainty," *Physics of Fluids*, vol. 27, no. 8, p. 085103, 2015.

12. A. P. Singh and K. Duraisamy, "Using field inversion to quantify functional errors in turbulence closures," *Physics of Fluids*, vol. 28, no. 4, p. 045110, 2016.

13. E. J. Parish and K. Duraisamy, "A paradigm for data-driven predictive modeling using field inversion and machine learning," *Journal of Computational Physics*, vol. 305, pp. 758–774, 2016.

14. M. Emory, J. Larsson, and G. Iaccarino, "Modeling of structural uncertainties in Reynolds-averaged Navier-Stokes closures," *Physics of Fluids*, vol. 25, no. 11, p. 110822, 2013.

15. A. Klein, K. Richter, A. Gardner, A. Altmikus, T. Lutz, and E. Krämer, "Numerical Comparison of Dynamic Stall for 2D Airfoils and an Airfoils Model in the DNW-TWG," in *Proc. European Rotorcraft Forum*, 2011, pp. 576–586.

16. W. C. Lawrence, K. W. McAlister, and W. J. McCroskey, "The Development of Dynamic Stall Based on Oscillating Airfoil Experiments," NASA Technical Note D-8382, 1977.

17. K. Richter, A. Pape, T. Knopp, M. Costes, V. Gleize, and A. Gardner, "Improved Two-Dimensional Dynamic Stall Prediction with Structured and Hybrid Numerical Methods," in *Proc. AHS Forum*, 2009.

18. G. Gori, O. Le Maître, and P. M. Congedo, "A confidence-based aerospace design approach robust to structural turbulence closure uncertainty," *Computers & Fluids*, vol. 246, p. 105614, 2022.

CLASSIFICATION & COPYRIGHT